Seeking TOA SW Flux Closure over ~~Synthetic~~ semi-Synthetic 3D Cloud Fields: Exploring the Accuracy of two Angular Distribution Models

Nils Madenach[1,2], Florian Tornow[3,4], Howard Barker[5], Rene Preusker[2], and Jürgen Fischer[2]

[1]Leibniz Institute for Tropospheric Research, Leipzig, Germany
[2]Freie Universität Berlin, Berlin, Germany, Emeritus
[3]Columbia University, New York, USA
[4]NASA Goddard Institute for Space Studies, New York, USA
[5]Environment and Climate Change Canada, Toronto, Ontario, Canada

Correspondence: Nils Madenach (nils.madenach@tropos.de)

Abstract. To accurately estimate outgoing top-of-atmosphere (TOA) shortwave (SW) fluxes from measurements of broadband radiances, angular distribution models (ADMs) are necessary. ADMs rely on radiance-predicting models that are trained on hemispherically-resolved CERES TOA radiance observations. The estimation of SW fluxes is particularly challenging for cloudy skies due to clouds' anisotropy, which substantially varies with their optical properties for any given sun-object-observer geometry. The aim of this study is to investigate ~~,~~ the influence of micro- and macrophysical properties of liquid clouds on SW fluxes estimated by ADMs that are based on a semi-physical model and compare to operational ADMs. We hypothesize that a microphysically-aware ADM performs better in observation angles influenced by single-scattering features.

The semi-physical ~~model relies on an optimized~~ approach relies on a parameterized asymmetry parameter $g^{\triangle}$ ~~that~~ , which depends on the cloud effective radius ~~. To improve the radiance prediction, $g^{\triangle}$ is adjusted for the different viewing geometries during the~~ and, after adjustments during training of the model, explicitly varies with sun–observer geometry. In this work, these adjustments are linked to single scattering features, such as the shift of the cloud bow and glory with varying cloud droplet ~~size.~~

sizes.

For the investigation~~synthetic~~ , 3D cloud scenes ~~based on observations~~ are constructed based on observational data and theoretical assumptions~~are created~~. Using a Monte Carlo ~~Model the TOA broad band~~ model, the TOA broadband SW radiances and fluxes of the ~~synthetic~~ semi-synthetic cloud scenes are simulated for different scenarios with varying viewing angles (~~θ_v~~θ_{v}) along the ~~principle~~ principal plane and solar angles (~~θ_s~~θ_{s}). Analyzing the scenarios, the sensitivity and accuracy of the two SW radiance-to-irradiance conversion approaches to cloud droplet size, spatial distribution of liquid water path, and mean optical thickness ~~is quantified.~~

are quantified.

The study emphasizes that ~~the inclusion of~~ explicitly including the liquid droplet effective radius in ~~the generation of ADMs can result in more accurate SW~~ ADM generation can improve the accuracy of shortwave flux estimates. Particularly for viewing geometries that exhibit single scattering phenomena, such as cloud glory and cloud bow, ~~instantaneous~~ flux estimates can benefit from microphysical-aware ADMs. For ~~instantaneous flux estimates~~the analyzed scenarios, we found that the ~~error in the~~ errors of instantaneous TOA SW flux estimates could be reduced by up to 25 ~~W/m^2. For cases~~ $\mathrm{Wm^{-2}}$. For scenes with very large or small droplets, the median error was reduced by up to 5 ~~W/m^2~~$\mathrm{Wm^{-2}}$.

1 Introduction

The Earth radiation budget (ERB) quantifies the overall balance of incoming solar radiation and outgoing reflected solar and emitted thermal radiation at the top of the atmosphere (TOA). Quantifying ERB is fundamental for understanding how the climate of Earth will change in the future. The main parameters influencing the ERB are the Earth's surface, clouds, aerosols, and atmospheric gases (e.g. Loeb and Manalo-Smith, 2005; Wild et al., 2014, 2018; Forster et al., 2021). ~~Outgoing~~ TOA outgoing radiative fluxes are estimated using, e.g., radiance measurements of broadband (BB) radiometers aboard polar orbiting and geostationary satellites (e.g. Viollier et al., 2009; Dewitte et al., 2008; Velázquez Blázquez et al., 2024a).

~~However, an accurate estimate of~~

However, accurately estimating the flux leaving Earth's TOA using only one measurement at a single sun-observer geometry, as is the case for satellites, is challenging. In particular, the reflected solar radiation can be highly anisotropic, depending on the observed scene. For clouds, ~~this dependency on the sun-observer~~ the dependency on sun–observer geometry is complex and ~~depends on the~~ governed by their macro- and microphysical ~~structure of the particles forming the cloud. In~~ properties. Over the past decades, ~~various approaches~~ a variety of radiance-predicting models have been developed and refined to estimate the anisotropy of ~~an observed cloudy scene~~ observed cloud scenes (e.g., Smith et al. (1986), Loeb et al. (2003), Loeb et al. (2005a), Su et al. (2015), Domenech and Wehr (2011), Tornow et al. (2021), Velázquez Blázquez et al. (2024b)). ~~These so-called angular~~ Using these distribution models (ADMs) ~~can then be used for a~~ the radiance-to-irradiance (flux) conversion ~~based on a single~~ can be achieved from a single satellite observation. An overview of different SW ADM approaches is given in Gristey et al. (2021).

In this study, we investigate TOA SW flux estimates for overcast marine liquid cloud scenes with varying macro- and microphysical properties. ~~For the SW flux estimates we use~~ SW fluxes are estimated using two sets of ADMs: one based on the semi-physical log-linear ~~approach (Tornow et al., 2020, 2021) , hereafter referred to as the~~ model (Tornow et al., 2020, 2021) (semi-physical approach~~. Furthermore, we estimate SW fluxes using the sigmoidal approach. This~~), and a second set derived using the state-of-the art sigmoidal approach (Su et al., 2015). The later is the currently operational approach used for SW flux estimates above clouds~~(Loeb et al., 2005b; Su et al., 2015), used, e.g., for SW flux estimates from~~, for example, by the Clouds and the Earth's Radiant Energy System (CERES). ~~Flux estimates based on the sigmoidal approach are also used as~~ The flux estimates from CERES are the input for the ~~Neural Network~~ ANN (Artificial Neural Network) approach, used in the EarthCARE ~~processor~~ BMA-FLX processor (Velázquez Blázquez et al., 2024b). To ~~explore~~ analyze the accuracy of the SW flux estimates and the sensitivity to ~~micro-and macrophysical propertiesthe results of Monte Carlo Simulations (MCS) performed on~~ micro- and macrophysical properties, 125 different 3D-cloud-scenarios are ~~investigated. Other than the sigmoidal approach, the~~ simulated using a Monte Carlo model. The semi-physical approach explicitly incorporates the mean cloud top effective radius (~~$\overline{r_{eff}}$)) via a~~ $\overline{r}^{\rm ctop}_{\rm eff}$) via the parametrized asymmetry parameter (~~$g^{\triangle}(\overline{r_{eff}})$~~$g^{\triangle}$), Tornow et al. (2020))~~that~~ , which also depends on the sun-observer ~~angular bin~~ angular-bin ($^{\triangle}$). ~~This workexplores~~ Within this work, the following main research questions are addressed:

1. How sensitive is the accuracy of TOA SW flux estimates to ~~varying~~ variations in effective radius, cloud homogeneity and optical thickness?
2. ~~Does~~ Can the explicit incorporation of cloud microphysics in a radiance-to-irradiance conversion approach improve the accuracy of SW flux estimates?
3. Are the adjustments of the asymmetry parameter $g^{\triangle}$ ~~due to~~ resulting from the optimization process ~~plausible~~ physically plausible, and what are the ~~specific~~ underlying causes for this?

~~In~~ Section 2 describes the theoretical basis of ADMs~~is described, the creation of the synthetic 3D-cloud scenesis explained~~ , the generation of 3D cloud scenes, and the configuration of the ~~MCS is given~~Monte Carlo model. In Section 3, the results are discussed, and in Section 4, the findings are summarized and concluded.

2 Theoretical Basis and Methodology

ADMs describe the hemispherically resolved deviation of ~~mean radiance $\overline{I}(\theta_s,\theta_v,\phi)$ reflected by a given scene~~ TOA angular-bin mean radiance $\overline{I}(\theta_{\rm s},\theta_{\rm v},\phi)$ from the isotropic case. The deviation is expressed through the anisotropic factor (R)~~where values larger~~ , where values greater than one indicate stronger reflection than ~~in~~ the isotropic case~~and vice versa~~, and values less than one indicate weaker reflection. Equation 1 describes how the anisotropic factor for a given solar zenith ~~θ_s~~$\theta_{\rm s}$, viewing zenith ~~θ_v~~ $\theta_{\rm v}$, and relative azimuth angle ϕ is calculated.

$$R(\theta_{\underline{s}\mathrm{s}},\theta_{\underline{v}\mathrm{v}},\phi) = \frac{\pi\overline{I}(\theta_s,\theta_v,\phi)}{\int_0^{2\pi}\int_0^{\frac{\pi}{2}}\overline{I}(\theta_s,\hat{\theta}_v,\hat{\phi})\cos(\hat{\theta}_v)\sin(\hat{\theta}_v)d\hat{\theta}_v d\hat{\phi}} \frac{\pi\,\overline{I}(\theta_{\rm s},\theta_{\rm v},\phi)}{\int_0^{2\pi}\int_0^{\pi/2}\overline{I}(\theta_{\rm s},\theta_{\rm v},\phi)\cos\theta_{\rm v}\,\sin\theta_{\rm v}\,d\theta_{\rm v}\,d\phi} \tag{1}$$

$$= \frac{\pi\overline{I}(\theta_s,\theta_v,\phi)}{\overline{F}(\theta_s)} \frac{\pi\,\overline{I}(\theta_{\rm s},\theta_{\rm v},\phi)}{\overline{F}(\theta_{\rm s})} \tag{2}$$

For a radiance observation ~~I_o~~ $I_{\rm o}$ at a given sun-observer geometry, the TOA flux estimates (~~$F(\theta_s)$) is~~ $F(\theta_{\rm s})$) are calculated using the anisotropic factor derived in Equation 1, following Equation 3.

$$F(\theta_{\underline{s}\mathrm{s}}) = \frac{\pi I_o(\theta_s,\theta_v,\phi)}{R(\theta_s,\theta_v,\phi)} \frac{\pi I_{\rm o}(\theta_{\rm s},\theta_{\rm v},\phi)}{R(\theta_{\rm s},\theta_{\rm v},\phi)} \tag{3}$$

~~Semi-physical approach~~

~~The~~

2.1 Sigmoidal approach

The currently operational approach to construct ADMs over marine clouds is described in, e.g., Su et al. (2015) and is an extension of the approach from Loeb et al. (2005a, b). For the approach, information of the CERES footprint average cloud optical depth $\overline{\tau}$ (exponential of the average over logarithmic τ values) and the cloud fraction f (in $\%$) is used to predict the hemispherical field of TOA SW radiances $\overline{I}$. Per angular-bin a sigmoidal function (4) is fitted to the observed CERES radiance I and $x = log(f \cdot \overline{\tau})$. Where solar irradiance I_0 as well as a, b, c, and x_0 are free parameters in the model.

$$I = I_0 + \frac{a}{[1 + e^{-(x - x_0)/b}]^c} \tag{4}$$

2.2 Semi-physical approach

As for the sigmoidal approach, the semi-physical approach uses ~~explicitly the microphysics of clouds and the~~ CERES footprint average cloud optical depth $\overline{\tau}$ and the cloud fraction f (here not in $\%$ but as fraction). Additionally, the semi-physical approach includes information of the cloud microphysics in the form of the footprint averaged effective radius ($\overline{r}_{\text{eff}}^{\text{ctop}}$) explicitly. Furthermore, the water vapor load above the clouds (above cloud water vapor, ~~ACWV) to predict the hemispherical field of outgoing TOA SW radiances $\overline{I}$ (see Fig. 1. Radiance ($\overline{I}$) predicted for a θ_s of 27 ° and an overcast scene over ocean with $\overline{\tau} = 10$. The three panels on the left show simulations using the semi-physical approach with variable r_{eff} and the right panel using the sigmoidal approach. The TOA SW anisotropy is~~ $ACWV$) is taken into account.

In Tornow et al. (2018) the TOA SW anisotropy has been found to be sensitive to both ~~variables and in~~ $\overline{r}_{\text{eff}}^{\text{ctop}}$ and $ACWV$. In the case of effective radius~~this can lead to~~, anisotropy differences of up to 8 $\%$ ~~(Tornow et al., 2018)~~were found. To incorporate these dependencies, ~~the semi-physical approach uses~~ a simple model (Eq. 5) relating the outgoing radiance I, to the incoming solar irradiance (~~S_0~~I_0) via a footprint albedo α and a factor describing the attenuation due to water vapor above clouds (e^{-2ACWV}) has been formulated. The factor 2 arises from the fact that the light passes the water vapor layer twice before reaching the TOA. By using the logarithm (Eq. 6) the model becomes linear and a simple first-degree polynomial function (Eq. 9) can be fitted to the observations.

$$I(\theta_{\underline{s}\mathrm{s}}, \theta_{\underline{v}\mathrm{v}}, \phi) \sim \underline{S_0} I_0 \cdot \alpha \cdot e^{-2 \cdot ACWV} \tag{5}$$

$$\log I(\theta_{\underline{s}\mathrm{s}}, \theta_{\underline{v}\mathrm{v}}, \phi) \sim \log \underline{S_0} I_0 + \log \alpha - 2 \cdot ACWV \tag{6}$$

The footprint albedo α (Eq. 7) is the sum of the clear sky portion of the scene (f_0) multiplied with the clear sky albedo (α^{cs}) and the cloud fraction (f_1) multiplied with the two-stream albedo (α_{ts}~~). α_{ts} (~~, Eq. 8). α_{ts} is the Coakley-Chylek approximation (Coakley and Chylek (1975)) and depends on the footprint mean cloud optical thickness ($\overline{\tau}$) and the ~~parametrized asymmetry~~

~~parameter~~ parameterized asymmetry parameter (g^{Δ}) for the given sun-observer bin~~($g^{\Delta}(\overline{r_{eff}})$).~~.

$$\alpha = f_0 \cdot \alpha_{\cancel{cs}\,\mathrm{cs}} + f_1 \cdot \alpha_{\cancel{ts}\,\mathrm{ts}} \tag{7}$$

$$\alpha_{\cancel{ts}\,\mathrm{ts}} = \cancel{\frac{\left(1 - g^{\Delta}(\overline{r_{eff}})\right) \cdot \overline{\tau}/2}{1 + (1 - g^{\Delta}(\overline{r_{eff}})) \cdot \overline{\tau}/2}} \frac{\left(1 - g^{\Delta}(\overline{r}_{\mathrm{eff}}^{\mathrm{ctop}})\right) \cdot \overline{\tau}/2}{1 + (1 - g^{\Delta}(\overline{r}_{\mathrm{eff}}^{\mathrm{ctop}})) \cdot \overline{\tau}/2} \tag{8}$$

Parameterized asymmetry parameter

The asymmetry parameter g in the two-stream albedo describes the tendency of radiation to scatter in the forward or backward direction. Symmetric scattering corresponds to $g = 0$, positive values ($g > 0$) to stronger forward scattering, and negative values ($g < 0$) to stronger backward scattering. g is a function of ~~the cloud microphysicsrepresented via the footprint mean cloud top~~ cloud microphysics, represented in this study by the footprint-mean cloud-top effective radius (~~$\overline{r_{eff}}$). During the training of the model, the asymmetry parameter has been optimized for each sun-observer~~ $\overline{r}_{\mathrm{eff}}^{\mathrm{ctop}}$), and is for marine liquid clouds about 0.86. In the semi-physical approach, g is optimized during model training for each sun–observer geometry bin (~~$^{\Delta}$) to improve the linearity between the observed radiances (see~~Δ) to reduce residuals. Due to this bin-wise optimization, the parameterized $g^{\Delta}(\overline{r}\mathrm{eff}^{\mathrm{ctop}})$ now also depends on the angular-bin Δ (see, e.g., Fig. 7, lower panel). ~~The bin-wise optimization of the asymmetry parameter $g^{\Delta}(\overline{r_{eff}})$ the α_{ts}~~ This optimization implicitly accounts for various ~~3D-effects that the model does not account for~~ 3D effects, as well as ~~single scattering features caused by~~ single-scattering features related to the underlying phase function~~as, e.g. the widening and shift towards the forward direction of cloud glory and a shift towards the direct backscatter~~, such as the broadening and forward shift of the cloud glory, and the shift of the cloud bow ~~with smaller $\overline{r_{eff}}$~~ toward the backscatter direction for smaller $\overline{r}_{\mathrm{eff}}^{\mathrm{ctop}}$ (e.g., Mayer et al. (2004)). ~~After the optimization the single scattering features became~~ With this new dependency, these single-scattering features become apparent in the ~~modeled radiances (see~~ radiances modeled using the semi-physical approach (see, e.g., Fig. 1 and Fig. 6). ~~An in depth explanation and further discussion of the~~

The semi-physical ~~approach are given in Tornow et al. (2018) and Tornow et al. (2020).For our investigation we will focus on overcast~~ model is fitted to the observations using an ordinary-least-square method with the free parameters A, B, C (Eq. 9).

$$\log I(\theta_{\mathrm{s}}^{\Delta}, \theta_{\mathrm{v}}^{\Delta}, \phi^{\Delta}) \approx \mathrm{A} + \mathrm{B} \cdot \log \alpha + \mathrm{C} \cdot ACWV \tag{9}$$

Throughout this study, only overcast ocean scenes ($f_1 = 1$) ~~above ocean with~~ with a clear-sky fraction set to zero ($f_0 = 0$~~and~~) and no above cloud water vapor ($ACWV = 0$~~. In order to provide angular coverage for the ADM construction,~~) are considered.

Figure 1 shows the predicted radiances using ADMs based on the sigmoidal approach (right panel) and on the semi-physical approach with varying $\overline{r}_{\mathrm{eff}}^{\mathrm{ctop}}$ (three left panels) and illustrates the sensitivity of the semi-physical approach to cloud microphysics. In the figure, both approaches agree best for a $\overline{r}_{\mathrm{eff}}^{\mathrm{ctop}}$ of 10 μm, which is in the range of average values found in marine boundary layer stratocumulus clouds. For decreasing $\overline{r}_{\mathrm{eff}}^{\mathrm{ctop}}$ the broadening of cloud glory and bow becomes apparent.

A detailed explanation and further discussion of the semi-physical approach can be found in Tornow et al. (2018, 2020, 2021).

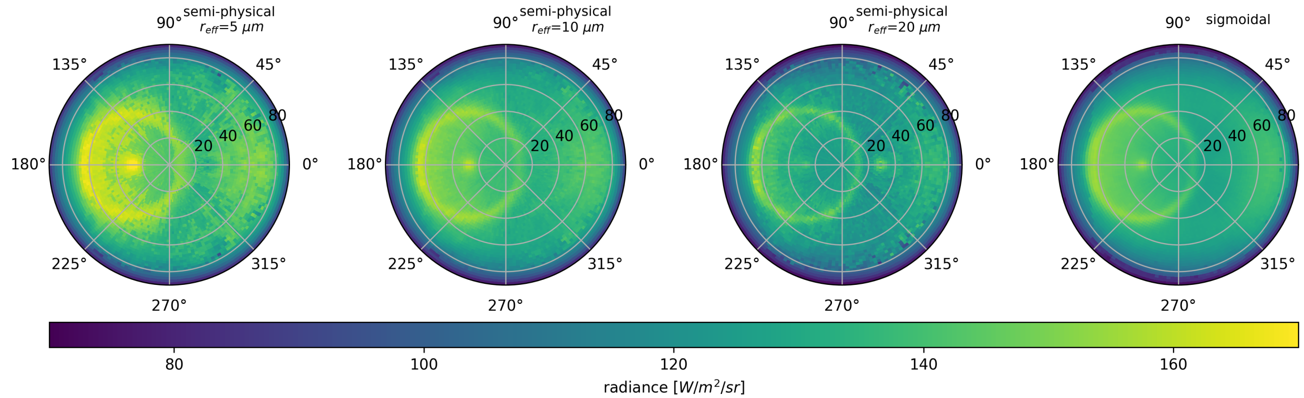

Figure 1. Radiance ($\overline{I}$) predicted for a θ_{s} of 27 ° and an overcast scene over ocean with $\overline{\tau} = 10$. The three panels on the left show simulations using the semi-physical approach with variable r_{eff} and the right panel using the sigmoidal approach.

For the creation of both sets of ADMs, the same CERES Ed4SSF (Edition 4.0 Single Scanner Footprint) observations between 2000 and 2005 ~~were usedwhen CERES~~ have been used. In this period, CERES aboard Aqua and Terra measured in the rotating azimuth plane scan mode, providing angular coverage for the ADM construction. The CERES Ed4SSF ~~(Edition 4.0 Single Scanner Footprint)~~ dataset of Aqua and Terra (described in Su et al. (2015)) ~~) that~~ combines MODIS and CERES L2 data~~has been used to collect observations for sun-observer~~. The observations were grouped into sun–observer bins ($^{\Delta}$) ~~of~~ spanning a 2° × 2° hemispherical grid. Only observations with more than 95% water surface, more than 0.1% cloud fraction, and solar zenith angles between 0° and 82° have been used. In the case of $ln(\overline{\tau}f) < 6$ (where f is in %) a look-up table approach has been used instead of sigmoidal fit in sun glint affected geometries (sun glint angle<20°~~×2°. To fit the collected data to the semi-physical model, an ordinary-least-square method has been usedwith the free parameters A, B, C (Eq. 9)~~). Further explanation on the selection of data and the methodology to fit the two approaches can be found in ~~Tornow et al. (2020).~~

~~$\log I(\theta_s^{\Delta}, \theta_v^{\Delta}, \phi^{\Delta}) \approx A + B \cdot \log \alpha + C \cdot ACWV$~~

~~Sigmoidal approach~~

~~The sigmoidal approach (Loeb et al., 2005b; Su et al., 2015) uses information of the CERES footprint average cloud optical depth $\overline{\tau}$ (exponential of the average over logarithmic τ values) and the cloud fraction f. Per angular bin a sigmoidal function (4)is fitted to the observed CERES radiance I and $x = log(f \cdot \overline{\tau})$.Where I_0, a,b, c, and x_0 are free parameters.~~

~~$I = I_0 + \frac{a}{[1 + e^{-(x - x_0)/b}]^c}$~~

Tornow et al. (2021). By using two extra retrieved parameters (r_{eff} and $ACWV$), the semi-physical approach is affected by additional retrieval uncertainties.

Table 1. Values used for the creation of cloud vertical profiles.

γ	Γ	~~k~~ k	~~A~~ D
1	1.5	0.8	0.0145

To explore the research questions raised above, 125 ~~realistic 30x30 km^2~~ semi-synthetical $30 \times 30\ \mathrm{km}^2$ 3D-cloud scenes with a horizontal resolution of 1 ~~km~~ km and varying mean optical thicknesses ($\overline{\tau}$), homogeneities (ν) and droplet number concentrations (~~N_d~~ N_d) are generated. The scenes are based on MODIS observations, and the vertical dimension is added using cloud adiabatic theory. The exact procedure is explained below.

2.3 Brief Recap on Cloud Adiabatic Theory

Following the adiabatic theory described, for example, in Brenguier et al. (2000) and Wood (2006), the vertical profile of cloud liquid water content (~~LWC~~ LWC) can be approximated by Equation 10. The mean cloud volume radius (~~r_{vol}~~ r_vol) for a given layer depends on the amount of liquid water in the layer ~~LWC~~ LWC and the concentration of cloud droplets (~~N_d~~ N_d). The effective radius (~~r_{eff}~~ r_eff) is related to ~~r_{vol}~~ r_vol via the constant k (see Equation 12).

$$\cancel{\mathrm{LWC}}LWC(z) = \gamma \cdot \Gamma \cdot z \tag{10}$$

$$r_{\cancel{vol}\mathrm{vol}} = \cancel{\frac{3\mathrm{LWC}}{4\pi\rho_w N_d}}\left(\frac{3LWC}{4\pi\rho_\mathrm{w} N_\mathrm{d}}\right)^{1/3} \tag{11}$$

$$r_{\cancel{eff}\mathrm{eff}} = \cancel{k}\mathrm{k}^{-1/3} \cdot r_{\cancel{vol}\mathrm{vol}} \tag{12}$$

Where ~~$z\,[m]$~~ $z\,[\mathrm{m}]$ is the height from cloud base, $\gamma\,[1]$ the degree of adiabaticity, ~~$\Gamma\,[g/m^3/m]$~~ $\Gamma\,[\mathrm{g\,m^{-3}\,m^{-1}}]$ the adiabatic rate of increase of liquid water content~~and $N_d\,[1/cm^3]$~~, and $N_d\,[\mathrm{cm^{-3}}]$ the cloud droplet number concentration. Following the equations above, the optical thickness τ of the cloud depends only on the geometrical thickness h and ~~N_d~~ N_d (see Equation 13).

$$\tau(h) = \cancel{A}\mathrm{D} \cdot (\gamma \cdot \Gamma)^{2/3} \cdot (\cancel{k}\mathrm{k} \cdot N_{\cancel{d}\mathrm{d}})^{1/3} \cdot h^{5/3} \tag{13}$$

where ~~A~~ D is a constant. Following Wood (2006), the cloud top effective radius (r_eff^{ctop}) has been calculated using:

$$r_\mathrm{eff}^{ctop}(h) = (\frac{3}{4}\pi\rho_\mathrm{w})^{1/3} \cdot (f \cdot \Gamma)^{1/3} \cdot (\mathrm{k} \cdot N_\mathrm{d})^{-1/3} \cdot h^{1/3} \tag{14}$$

The values used for the parameters and constants are shown in Table 1.

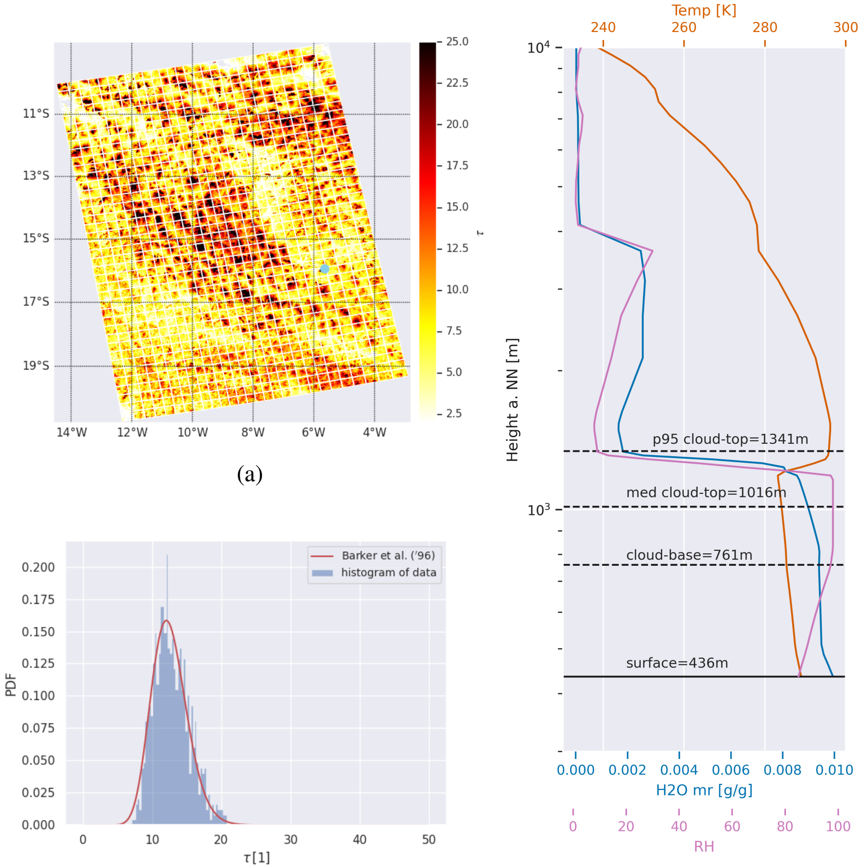

(a)

(b)

(c)

Figure 2. (a) MODIS retrieved τ above south-east Atlantic on September 5th, 2014. The frame is separated into 30×30 km^2 boxes. The blue dot denotes the location of St. Helena. (b) Example of a gamma distribution of τ (red line) following Barker et al. (1996) generated using $\overline{\tau} = 12.6$ and $\nu = 24.1$ from a 30×30 km^2 box of the MODIS frame. In blue the histogram of the τ values within the box is displayed. (c) Vertical profiles of T, relative humidity (RH) and H_2O mixing ratio from radiosonde ascent at St. Helena from September 5th, 2014 at 12 p.m. LT. The dashed black lines indicate the cloud base and the 50th and 95th percentile of cloud tops for all 125 scenes.

2.4 Creation of ~~Synthetic~~ semi-Synthetic 3D-Cloud Scenes

For the creation of the ~~scenes~~ cloud scenes, we analyzed a MODIS frame from September ~~5th~~ 5, 2014~~above~~, in the south-east Atlantic~~covered with~~, covered by marine boundary layer ~~Stratocumulus clouds.~~ stratocumulus clouds (Fig. 2 (a)). ~~To~~ In order to obtain realistic ranges of mean cloud optical thickness $\overline{\tau}$ and homogeneities ν in marine boundary layer clouds, we separated the MODIS frame into ~~30x30 km^2 boxes~~30×30 km^2 boxes, as shown in Fig. 2 (a). For each box, we calculated $\overline{\tau}$ following

Equation 15 and ν following Equation 16.

$$\overline{\tau} = \exp(\overline{\log(\tau)}) \tag{15}$$

$$\nu = \left(\frac{\overline{\tau}}{std(\tau)}\right)^2 \tag{16}$$

~~For the boxes within the MODIS frame, we found values~~ We found a value range of $\overline{\tau}$ ~~values~~ between 2.8 and 20.1 and of ν ~~values~~ between 2 and 26.

For the creation of idealistic cloud scenes, gamma functions based on Barker et al. (1996) have been used to calculate PDFs of optical thickness values for the given $\overline{\tau}$ and ν pair of the scene (see Fig. 2 (b)). In total, 25 PDFs have been created based on five $\overline{\tau}$ values (2.8, 4.5, 7.4, 12.2, 20.1) and five ν values between 2 and 26. In the next step, the idealistic range of τ values (p<0.001) for the given $\overline{\tau}$ and ν was extracted from each PDF and the cloud geometrical thickness h using Equation 13, was calculated for each τ~~bin~~ -bin within the range.

Assuming a constant cloud base and ~~N_d~~N_{d}, the optical thickness τ depends only on the cloud top height (Eq. 13). Using Equation 10 to 12 vertical profiles of ~~LWC and r_{eff}~~ LWC and r_{eff} are calculated for ~~grid-cell of the scenarios~~each τ-bin. The vertical resolution of the profiles is set to 25 ~~m~~m. For the stratocumulus deck of the MODIS frame (Fig. 2 a)), a very similar cloud base is assumed. Using radiosonde measurements of T, and water vapor at 12 p.m. LT in St. Helena, a cloud base of 761 ~~m~~ m was assumed (see Fig. 2 (c)). To obtain a realistic spatial distribution of ~~the~~ cloud profiles, we ~~assigned them to MODIS boxes with~~ found for each scene, the MODIS box with the most similar $\overline{\tau}$ and ν ~~and used~~ values. The profiles are than allocated to the spatial distribution of the τ values within the box~~to assign the profiles~~. Table A1 summarizes the pre-defined $\overline{\tau}_{\mathrm{pre}}$ and ν_{pre} of the scenes, as well as the calculated values ($\overline{\tau}$, ν, and $\overline{r}_{\mathrm{eff}}^{\mathrm{ctop}}$) after assigning them to the MODIS boxes with the most similar values ($\overline{\tau_o}$ and ν_o).

Applying five different ~~N_d's~~ N_{d}'s of 25, 50, 100, 200, and 400~~$1/cm^3$,~~ $[\mathrm{cm}^{-3}]$ resulted in 125 scenes with $\overline{r}_{\mathrm{eff}}^{\mathrm{ctop}}$ values ranging from 5.1 to 22.1 μm. Figure 3 and 4 display the results, showing the geometrical thickness h of the clouds for ~~the~~ a range of $\overline{\tau}$ and ν and for a ~~N_d~~ N_{d} of 25 ~~$[1/cm^3]$~~ $[\mathrm{cm}^{-3}]$ and 400 ~~$[1/cm^3]$ respectively.~~ $[\mathrm{cm}^{-3}]$ respectively. The values in red represent the calculated $\overline{\tau}$, ν and $\overline{r}_{\mathrm{eff}}^{\mathrm{ctop}}$ after assigning (see also Table A1). Comparing Fig. 3 and ~~Fig. 4we see,~~ 4, we see that to reach the same τ, the cloud extend must be larger for larger cloud droplets (smaller ~~N_d). This is because smaller particles (larger N_d) scatter the light stronger in the backward direction, leading to stronger attenuation.~~ N_{d}).

2.5 Monte Carlos Simulations

The 125 ~~synthetic~~ semi-synthetic scenes of cloud fields are used as inputs for a Monte Carlo Model (Marchuk et al., 1980; Barker et al., 2003) to simulate the SW TOA radiances and calculate TOA SW fluxes. For the simulations, cyclical boundary conditions are assumed. For each scene, simulations for 40 viewing zenith angles between -77 to 77° along the ~~principle~~ principal plane and for solar zenith angles of 1, 27, 55, and 75° ~~has~~ have been performed. In total, this resulted in 20 000 scenarios. For each simulation, 10^7 photons have been used. The ocean surface is Lambertian ~~(corresponding to a near-surface wind speed of 0 m/s in ADMs) with~~ with a wavelength independent albedo of 0.05. For the hydrometeors, Mie-phase functions

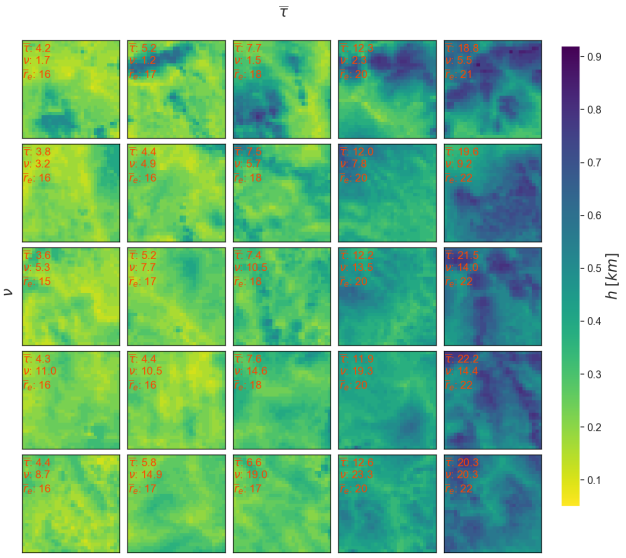

Figure 3. Cloud geometrical thickness for the 25 scenes with varying $\overline{\tau}$ and ν and with the N_d set to 25 $[\mathrm{cm}^{-3}]$. The numbers in red represent the scene-averaged values, calculated after assigning the generated profiles to the MODIS boxes.

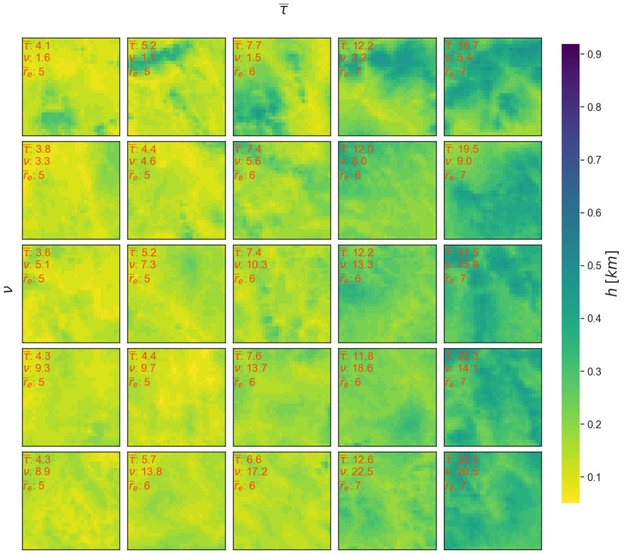

Figure 4. Same as Fig. 3 but with N_d of 400 $[\mathrm{cm}^{-3}]$

with 1800 ~~angular bins~~ angular-bins are used. The spectrally-dependent optical properties are computed with the model used in EarthCARE's ACM-RT product (Cole et al. (2023)).

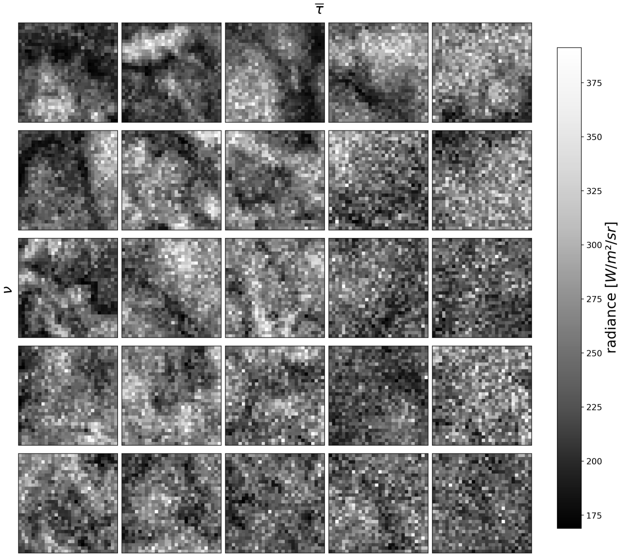

Figure 5. Monte Carlo simulations of TOA radiances for scenes ~~with $N_d = 400$~~ in Fig. 4 and for ~~$\theta_v = -29°$~~ $\theta_\mathrm{v} = -29°$ and ~~$\theta_s = 27°$~~$\theta_\mathrm{s} = 27°$.

In order to investigate the contribution of single scattering to the outgoing TOA radiance (research question 3), a histogram of the weighted fraction of the number of scattering events has been stored from the simulation for each scenario.

~~(a) MODIS retrieved τ above south-east Atlantic on September 5th, 2014. The frame is separated into 30x30 km^2 boxes. The blue dot denotes the location of St. Helena. (b) Example of a gamma distribution of τ (red line) following Barker et al. (1996) generated using $\overline{\tau} = 12.6$ and $\nu = 24.1$ from a 30x30 km^2 box of the MODIS frame. In blue the histogram of the τ values within the box is displayed. (c) Vertical profiles of T, relative humidity (RH) and H_2O mixing ratio from radiosonde ascent at St. Helena from September 5th, 2014 at 12 p.m. LT. The dashed black lines indicate the cloud base and the 50th and 95th percentile of cloud tops for all 125 scenes. Cloud geometrical thickness for the 25 scenes with varying $\overline{\tau}$ and ν and with the N_d set to 25 $[1/cm^3]$ Same as Fig. 3 but with N_d of 400 $[1/cm^3]$~~

3 Results

In addition to flux estimates based on ADMs using the semi-physical approach ~~, we use flux estimates based on ADMs using~~ (Sec. 2.2), fluxes based on the currently operational ~~sigmoidal approach~~ADMs (Sec. 2.1), reconstructed in Tornow et al. (2021) and based on Su et al. (2015), are estimated. In contrast to the semi-physical ~~approach, the sigmoidal approach does~~ ADMs, the currently operational ADMs do not explicitly take into account the cloud droplet effective radius. ~~Further description of this method can be found, for example, in Loeb et al. (2005b), Su et al. (2015) and Gristey et al. (2021).~~ ~~In~~ The estimated fluxes are compared against Monte Carlo simulations. Fig. 5 ~~an example of the results from the Monte Carlo Simulations is shown. Using the scene averaged radiances as I_o (see Fig. 6), fluxes are estimated for all scenarios using both approaches~~illustrates

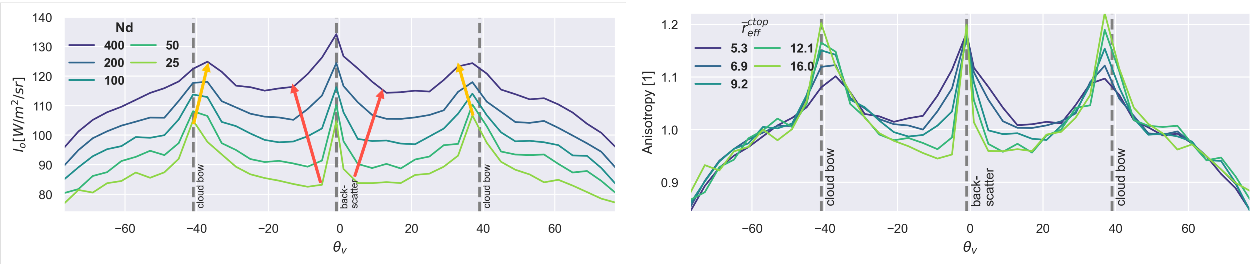

Figure 6. Upper panel: Mean radiance of the MCS used as ~~I_o~~ I_o along ~~θ_v~~ θ_v (~~principle~~ principal plane) and for varying ~~N_d~~ N_d. For a ~~$\theta_s = 1^\circ$~~ $\theta_\mathrm{s} = 1^\circ$ and for the scene with ~~$\overline{\tau} = 2.8$~~ $\overline{\tau}_\mathrm{pre} = 2.8$ and ~~$\nu = 8$~~ $\nu_\mathrm{pre} = 8$. The vertical lines indicate the location of single scattering phenomena as the cloud bow and cloud glory (around the direct backscatter). Yellow arrows indicate the shift of the cloud bow towards the direct backscatter and red arrows the ~~widening~~ broadening of the cloud glory with smaller droplets (higher N_d). Lower panel: corresponding anisotropy values for the different N_d but here expressed via the the mean cloud top effective radius $\overline{r}_\mathrm{eff}^\mathrm{ctop}$ of the scene.

Monte Carlo simulated radiances for all scenes with $N_\mathrm{d} = 400\,[\mathrm{cm}^{-3}]$ and for $\theta_\mathrm{v} = -29^\circ$ and $\theta_\mathrm{s} = 27^\circ$.

Figure 6 displays the ~~mean radiance for one scene ($\overline{\tau} = 2.8$ and $\nu = 8$) at $\theta_s = 1^\circ$ and for different N_d~~ Monte Carlo simulated and scenario-averaged radiances $I_\mathrm{o}(\theta_\mathrm{s}, \theta_\mathrm{v}, \phi)$ (upper panel) and corresponding anisotropies (lower panel) at $\theta_\mathrm{s} = 1^\circ$ along the principal plane and for all scenes with $\overline{\tau}_\mathrm{pre} = 2.8$ and $\nu_\mathrm{pre} = 8$ (see Table A1) and for different N_d. We see ~~large differences in the reflected radiation by only changing the microphysical property of the~~ the strong dependency of the reflected radiation from the mean cloud droplet size. We also observe single scattering features ~~become~~ becoming apparent, such as the broadening of the cloud glory and the shift of the cloud bow towards the direct ~~backscatterer~~ backscatter with decreasing droplet size (increasing ~~N_d~~ N_d).

ADMs based on the sigmoidal and semi-physical approaches are constructed using the scene-averaged cloud parameters $\overline{\tau}$ for the former, and additionally $\overline{r}_\mathrm{eff}^\mathrm{ctop}$ for latter (see Sec. 2.2 and 2.2). All scenes are overcast ($f = 1$) and have $ACWV = 0$. With the resulting anisotropies R, SW fluxes are estimated using the spatially averaged Monte Carlo simulated radiances $I_\mathrm{o}(\theta_\mathrm{s}, \theta_\mathrm{v}, \phi)$ (see Fig. 5).

The upper panel of Fig. 7 shows the TOA SW fluxes across the ~~principle~~ principal plane for scenarios with a solar zenith angle of 1° and scenes with ~~a~~ an optical thickness of $\overline{\tau}$ = 7.4 and homogeneity of ν = 20. The solid lines show the "true" fluxes from the Monte Carlo simulations. The dashed lines represent the flux estimates based on the semi-physical approach (F_sp), and the dotted lines ~~the~~ flux estimates based on the sigmoidal approach (F_sig). The colors of the lines illustrate estimates for scenes with different ~~droplet number concentrations N_d~~ cloud effective radii. In addition, the colored dots indicate the weighted fraction of photons of the scenario that experienced single scattering before reaching TOA. The lower panel illustrates the parameterized asymmetry parameter g^Δ used for the semi-physical ADMs. The vertical lines show the location of the cloud bow and the direct backscatter, around which the cloud glory forms. The results show that ~~an increase of N_d from 25 to 400 $1/cm^3$~~ a decrease of $\overline{r}_\mathrm{eff}$ from 16 to 5.3 μm produces up to 100 ~~W/m^2~~ $\mathrm{W m^{-2}}$ higher fluxes at TOA for the same $\overline{\tau}$.

Around the direct backscatter direction, where the cloud glory contributes to the observed radiance~~of the scenes~~, the ADMs

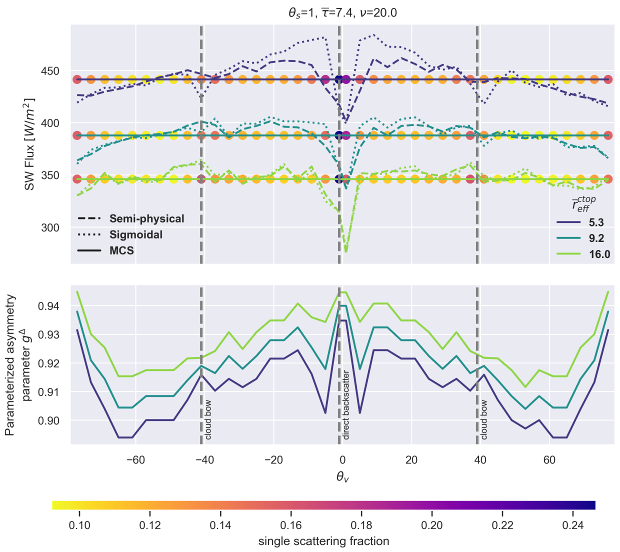

Figure 7. Upper panel: Flux estimates using ADM based on the semi-physical (dashed) and based on the sigmoidal (dotted) approach for different droplet number concentrations along the ~~principle~~ principal plain. The true flux of the Monte Carlo Simulations (MCS) is shown in the solid line. The colored dots represent for each scenario the fraction of photons that has been scattered only once. Lower panel: parametrized asymmetry parameter g^{Δ} used for semi-physical approach.

~~created~~ generated using the semi-physical approach result in flux estimates that are closer to the ~~MCS~~simulations. This is also the case at the cloud bow around +-40°. ~~Especially for~~ Particularly for small droplet sizes (high droplet number concentrations~~(small droplet sizes~~), where the enhanced reflectance due to single scattering effects ~~are~~ is largest, the currently operational approach underestimates the fluxes. Due to the bin-wise ~~parametrized~~ optimized asymmetry parameter (bottom panel), the semi-physical approach is able to capture single scattering features ~~as the widening and shift towards~~ such as broadening and shift in the forward direction of the cloud glory, as well as the shift towards the direct backscatter of the cloud bow with ~~increasing N_d~~ decreasing $\overline{r}_{\mathrm{eff}}$ (Tornow et al., 2021). The results illustrate that this leads to more accurate flux estimates in these geometries ~~in comparison~~ comparing to the sigmoidal approach.

For angles influenced by the cloud bow or cloud glory, an enhanced contribution of single scattering (colored dots) to the reflected radiance is clearly visible. Furthermore, the single scattering fraction increases with ~~increasing N_d~~decreasing $\overline{r}_{\mathrm{eff}}$. This underpins the hypothesis ~~,~~that the adjustments of g^{Δ} (lower panel) during the ~~bin wise~~ bin-wise optimization procedure (Tornow et al., 2020) ~~, are primarily due~~ are primarily attributable to perceived single scattering effects~~as, e.g., the widening~~ , such as the broadening and shift of the cloud glory and the shift of cloud bow.

Figure 8 shows the results for ~~θ_s~~ θ_{s} for 27° and 55° with similar results. At geometries influenced by the cloud glory, the sigmoidal approach performs well under average microphysical conditions (e.g, ~~$N_d = 100$~~$\overline{r}_{\mathrm{eff}} \approx 10\mu\mathrm{m}$) but overestimates ~~at low and underestimates at high N_d the fluxes~~the fluxes at high and underestimates them at low $\overline{r}_{\mathrm{eff}}$. This agrees with Fig. 1 where the predicted radiances using the sigmoidal approach (right panel) correspond well with the semi-physical approach

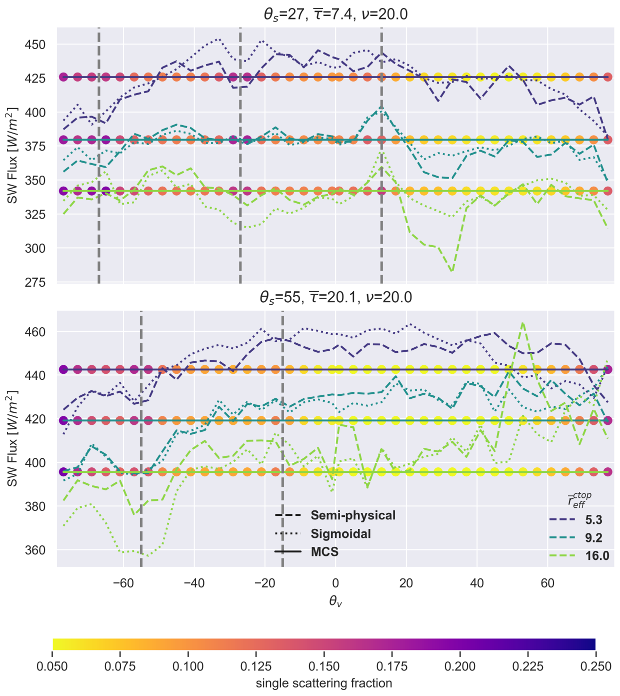

Figure 8. As Fig. 7 upper panel but for a ~~θ_s~~ θ_{s} of 27° and 55°

using a typical mean effective radius of 10 ~~μm~~ μm (second panel) but ~~is~~ are lower for small droplets (first panel) and higher for large droplets (third panel).

At high and low ~~θ_v~~ θ_{v}, both approaches struggle because fewer training data ~~were~~ was available for these geometries. In sun-glint affected ~~angles~~ geometries both approaches have problems in ~~accurately estimate~~ estimate accurately the fluxes, but the semi-physical approach generally deviates even more. These findings are consistent with ~~larger~~ higher uncertainties of the models for these geometries found in Tornow et al. (2020).

In Fig. 9, the flux deviations for scenes with a ~~N_d~~ N_{d} of 400 ~~$1/cm^3$~~ cm^{-3} and the corresponding highest homogeneity are illustrated for varying $\overline{\tau}$ and ~~θ_s~~ θ_{s}. The upper panel ~~shows~~ displays the deviation of the flux estimates using semi-physical (ΔF_{sp}) and the lower panel using sigmoidal based ADMs (ΔF_{sig}). In the top of each panel~~the mean~~, the average over all $\overline{\tau}$ (black line) and the standard deviation (gray shadows) are shown. The doted isoline indicates areas where the differences exceed the EarthCARE mission goal of ±10 ~~W/m^2~~ $\mathrm{Wm^{-2}}$.

~~We see that generally~~ In general, the semi-physical approach deviates less ~~, especially for viewing-geometries~~ from the simulations, particularly in viewing geometries around the cloud glory and cloud bow. This is the case for all optical thicknesses and solar zenith angles, but for small ~~optical thicknesses~~ $\overline{\tau}$ the effect is more distinctive. The deviations in instantaneous flux estimates using the semi-physical approach compared to the currently operational approach can be reduced by up to 25 $\mathrm{Wm^{-2}}$ or even more~~W/m^2~~. In the sun glint affected ~~regions~~ geometries, both approaches show large uncertainties. Both absolute and relative deviations (not shown) increase with smaller $\overline{\tau}$ in this region. This indicates that even in overcast cases, with high optical thicknesses, the sun-glint significantly influences the TOA radiances~~and the ADMs are not able to accurately account for this~~. Figure 10 illustrates the box-whisker plots (~~n=2000~~$\mathrm{n=2000}$) of flux deviations (ΔF) for scenarios in the backward (left)

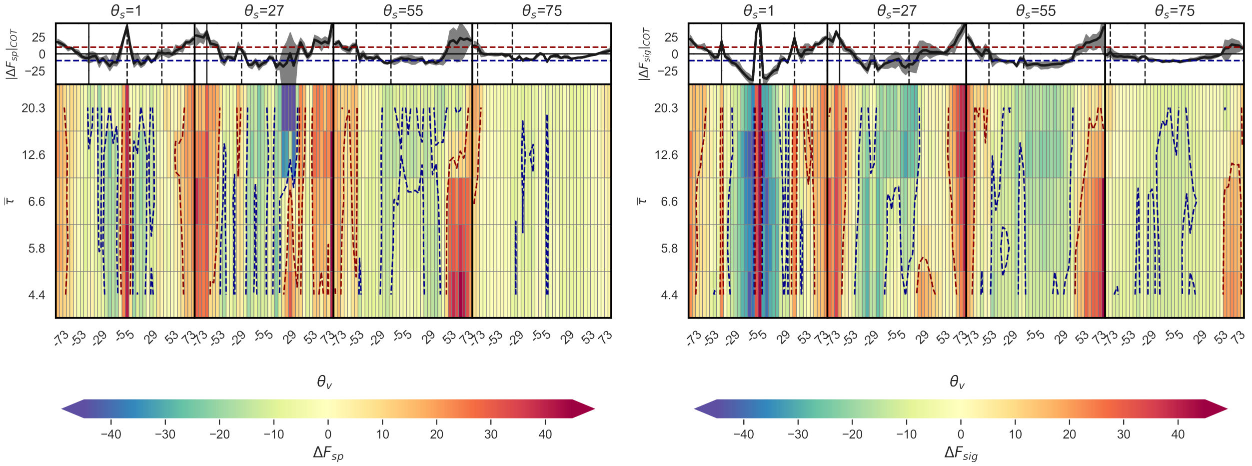

Figure 9. Deviation of fluxes estimated (~~$\Delta F = F_{MCS} - F_{est}$~~$\Delta F = F_{\mathrm{MCS}} - F_{\mathrm{est}}$) using ADM's based on the semi-physical approach (upper panel) and on the sigmoidal approach (lower panel) from the fluxes of MCS along the ~~principle~~ principal plane and for varying ~~θ_s~~ θ_{s} and $\overline{\tau}$. The ~~N_d~~ N_{d} of the scenes is 400 ~~$[1/cm^3]$~~ $[\mathrm{cm^{-3}}]$ and for ν always the scene with the highest homogeneity is selected. The dotted blue and red lines represent the -10 and 10 ~~W/m^2~~ $\mathrm{Wm^{-2}}$ threshold. On top of each panel the deviation averaged over all optical thicknesses is shown. The shaded areas mark the 5th and 95th percentiles. The vertical lines indicate the direct backscatter and the cloud bow (~~$\theta_s \pm 40°$~~$\theta_{\mathrm{s}} \pm 40^\circ$).

and forward direction (right), and for different droplet number concentrations. ~~The flux estimates based on the semi-physical approach deviates from the simulations in the backward direction. Especially, at extreme N_d~~ Particularly at extreme N_{d} (e.g., ~~5~~ 25 cm^{-3} and 400 cm^{-3}), the semi-physical approach deviates less from the simulations in the backward direction. The median deviation of the 2000 scenarios can be reduced by up to 5 ~~W/m^2~~$\mathrm{Wm^{-2}}$. This can be explained by the fact that the sigmoidal approach does not explicitly take ~~N_d~~ N_{d} into account. By using observations independently on their microphysics, the sigmoidal approach produces best estimates at average ~~N_d of, e.g.~~ N_{d} such as 50 and 100 ~~$1/cm^3$~~$\mathrm{cm^{-3}}$, but is less accurate in extreme high or low ~~N_ds~~$N_{\mathrm{d}}s$. Table 2 lists the probability of ~~$\Delta F > 10\ W/m^2$~~ $\Delta F > 10\,\mathrm{W/m^2}$ for scenes with different ~~N_d~~ N_{d} and for scenarios calculated for the ~~Backward, Forward and Nadir~~ backward, forward and nadir direction. For high ~~N_d~~ N_{d} the semi-physical approach can reduce the probability by up to 20 %. ~~We found that in general the~~ The mean absolute relative error ~~decreases~~ was found to decrease with increasing $\overline{\tau}$ and ν~~and increases with increasing θ_s andespecially~~, and to increase with larger θ_{s} and, particularly for the sigmoidal approach~~with increasing N_d~~, with decreasing $\overline{r}_{\mathrm{eff}}^{\mathrm{ctop}}$ (increasing N_{d}) (not shown).

In Fig. 11 the ~~$30{\times}30km^2$ scene has~~ $30\times30\,\mathrm{km}^2$ scenes have been divided into subdomains with sizes of 25, 20, 15 and 10 ~~km~~km to explore the dependency of the flux estimates on domain size . The variability in ΔF increases with smaller

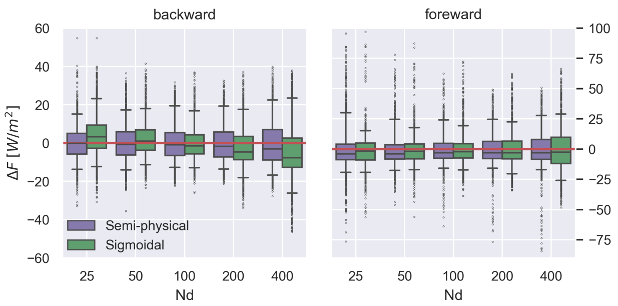

Figure 10. Box-Whisker plots showing flux deviations using ~~$n = 2000$~~ $n = 2000$ scenes of all ~~θ_s~~θ_s, $\overline{\tau}$, ν and for the left panel of ~~$-77 < \theta_v < 0$~~ $-77 < \theta_\mathrm{v} < 0$ and for the right panel ~~$0 < \theta_v < 77$~~$0 < \theta_\mathrm{v} < 77$. The upper and lower limits represent the 95th and 5th percentiles.

~~Nd~~ N_d	Forward	Backward	Nadir
25	35.2/34.1	23.0/31.5	39.5/38.5
50	33.7/31.0	27.0/23.9	41.0/33.0
100	34.0/31.5	27.1/24.3	37.0/31.0
200	36.7/42.8	31.0/35.1	38.0/43.5
400	43.8/58.2	41.0/55.8	58.5/79.5

Table 2. Table showing the probability in % of ~~$\Delta F > 10\ W/m^2$~~$\Delta F > 10\,\mathrm{W/m^2}$. Forward includes all scenarios of ~~$0 < \theta_v < 77$~~$0 < \theta_\mathrm{v} < 77$, backward of ~~$0 > \theta_v > -77$~~ $0 > \theta_\mathrm{v} > -77$ and nadir of ~~$-1 < \theta_v < 1$~~$-1 < \theta_\mathrm{v} < 1$. The purple numbers are for the semi-physical approach and green numbers for the sigmoidal approach.

domain sizes. As in the case of 30 ~~km~~km, the semi-physical approach produces better estimates in the backward direction and for domains with extremely high or low ~~N_d~~ $\overline{r}_\mathrm{eff}^\mathrm{ctop}$ (N_d) for all resolutions. For a domain size of ~~10 km~~ $10 \times 10\,\mathrm{km}^2$ both approaches show a positive bias. As EarthCARE's assessment domain has ~~also~~ a size of 100 ~~km^2. The~~ km^2, the results might be of interest for the validation of the BMA-FLX product.

4 Conclusion and Discussion

In this study, Top of Atmosphere (TOA) short wave (SW) radiances are simulated along the principal plane for 125 ~~synthetic~~ semi-synthetic 3D ~~cloud scenes with varying~~ scenes of marine boundary layer stratocumulus clouds with varying mean cloud optical thickness, cloud homogeneities~~and cloud droplet number concentration~~, and mean effective radius. Seeking TOA SW flux closure above liquid clouds, two ~~ADMs namely~~ sets of ADMs based on the semi-physical ~~(Tornow et al., 2021)~~

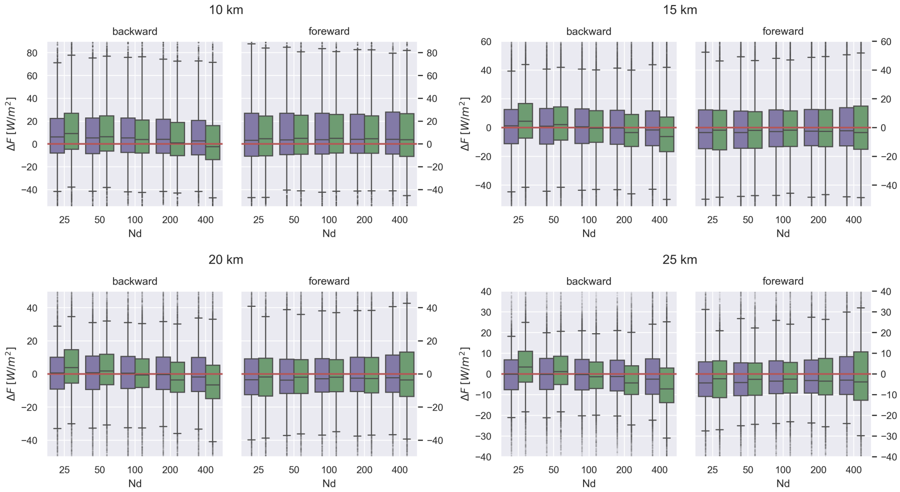

Figure 11. As Fig. 10 but for domain sizes of 25, 20, 15 and 10 ~~km~~km.

(Tornow et al., 2021, 2020) and sigmoidal approach (Su et al., 2015) ~~,~~ are compared against the fluxes calculated using ~~the~~ a Monte Carlo Model ~~.~~

~~We found that in general~~ (Marchuk et al. (1980), Barker et al. (2003)). Averaged over all analyzed scenarios the mean absolute relative error decreases with increasing $\overline{\tau}$ and ν and increases with increasing ~~θ_s andespecially~~ θ_s and, particularly for the sigmoidal approach~~with increasing N_d~~, with decreasing $\overline{r}_\mathrm{eff}^\mathrm{ctop}$ (Research question 1).

~~The~~ Furthermore, the microphysical-aware semi-physical approach reduces the errors in instantaneous flux estimates by up to 25 ~~W/m^2~~ $\mathrm{Wm^{-2}}$ compared to the sigmoidal approach. The improvements are found to be largest for geometries in the backward direction and for scenes where microphysics ~~deviates~~ deviated most from mean conditions~~as e.g., for~~ , such as for scenes with extremely high or low ~~N_d~~$\overline{r}_\mathrm{eff}^\mathrm{ctop}$ (N_d). The median deviation ~~($n = 2000$)~~ of these scenarios (backward direction and different ~~N_d~~N_d, n = 2000) is improved for all ~~N_d~~ N_d by up to 5 ~~W/m^2. The results are in agreement with a study from Tornow et al. (2021)comparing~~ $\mathrm{Wm^{-2}}$. Although this study only covers the principal plane, the results show the potential of improving SW flux estimates by explicitly incorporating cloud microphysics in ADMs. Similar results have been found in Tornow et al. (2021), where the two radiance-to-irradiance approaches have been compared using satellite data (Research question 2).

Analyzing the Monte Carlo Simulations (MCS), the adjustments of the parameterized asymmetry parameter g^Δ ~~used in due to the optimization~~ could be related to changes in the fraction of single scattering events contributing to the TOA radiance signal. The changes in the single scattering fraction are associated with phenomena such as cloud bow or cloud glory that depend on cloud microphysical properties (Research question 3).

By explicitly incorporating cloud microphysical properties ~~,~~through the effective radius, the semi-physical approach substantially reduces ~~errors in flux estimates, particularly in scenarios affected by single scattering phenomena , such as~~ flux estimation errors for the investigated scenarios, particularly for those affected by single-scattering phenomena such as the cloud glory and the cloud bow. As these phenomena are strongest in the backward direction, the improvements compared to the currently operational approach are most pronounced in scenarios with corresponding ~~angles. For sun-glint affected observations~~observational geometries. For sun glint affected geometries, the flux estimates show large variabilities and ~~larger errors and should therefore be interpreted~~ any interpretation should be done with caution.

Using the optimized g^{Δ}, the semi-physical approach is able to capture the shift of the cloud bow and the ~~widening~~ broadening of the cloud glory with decreasing droplet size, explaining the more accurate estimates in these geometries.

~~The findings in~~

The findings of this study encourage ~~the additional use of the semi-physical approach for the EarthCARE mission~~further research on microphysics-aware ADMs. For the radiative closure experiment of the EarthCARE mission, launched in May 2024 (Wehr et al., 2023)~~. The mission performs a radiative closure experiment~~ , the semi-physical approach shows potential to improve SW flux estimates. EarthCARE aims to achieve radiative closure by comparing simulated fluxes ~~, based on measurements~~ from active and passive instruments aboard the satellite ~~, with estimated fluxes, based on measurements from a broadband radiometer (Velázquez Blázquez et al., 2024b). Especially for viewing~~ with estimates from the broadband radiometer (BBR) (Velázquez Blázquez et al., 2024b). Particularly for observational geometries in the ~~backward scattering~~ backward-scattering direction, the semi-physical approach ~~might help to reduce~~ reduces potential misinterpretations of flux deviations ~~in the closure that are larger than~~ that exceed the mission goal of 10 ~~W/m^2, but that actually are due to~~ $\mathrm{Wm^{-2}}$, but actually arise from uncertainties in the SW flux estimates. ~~When seeking the radiative closure for EarthCARE, we should always be aware that the~~ Although EarthCARE's observational geometries lie outside the principal plane investigated in this study (e.g., Tornow et al. (2019)), they are likewise influenced by variations in cloud microphysics and single-scattering phenomena. When assessing radiative closure with EarthCARE, it is important to remember that BBR-based fluxes are estimates ~~and not measurementsand have uncertainties that vary depending~~ rather than direct measurements, and that their uncertainties depend on surface type, atmospheric conditions, and ~~sun-satellite angles. Especially for high N_d~~ sun–satellite geometry. For low $\overline{r}_{\mathrm{eff}}^{\mathrm{ctop}}$ (high N_{d}), the semi-physical approach substantially reduces the probability of ~~$\Delta F > 10\ W/m^2$ substantially~~$\Delta F > 10\ \mathrm{Wm^{-2}}$. For both approaches, ~~the flux uncertainties increased with smaller~~ flux uncertainties increase with decreasing footprint size.

Future work should further investigate the sensitivities to footprint size, retrieval errors (e.g., of above-cloud water vapor and r_{eff}), noise, and varying observational conditions.

Overall, the ~~study indicates that incorporating information on cloud microphysical properties into the development of~~ results highlight that explicitly incorporating cloud microphysical information into ADMs is a promising pathway for ~~enhancing~~ improving TOA SW flux estimates above clouds. ~~In contrast to previous ERB missions , which primarily focused on minimizing the global bias of flux estimates, EarthCAREis designed with an~~ Unlike previous Earth radiation budget missions that focused mainly on minimizing global flux biases, EarthCARE's emphasis on radiative closure ~~and~~ may particularly benefit from ~~microphysical-aware~~ microphysics-aware instantaneous flux estimates. ~~The results presented encourages further study on e.g., sensitivity to the accuracy of the physical retrievals, to noise, and observational conditions.~~

Author contributions. FT, NM and HB designed the study. NM created the input scenes, performed the analysis and wrote the paper. HB carried out the Monte Carlo Simulations. RP and JF supervised the work.

Competing interests. The authors declare that they have no conflict of interest.

Acknowledgements. We thank the reviewers for their constructive and valuable feedback. Language refinement and grammar correction were assisted by AI-based tools. The authors are solely responsible for the scientific content and conclusions. This research has been supported by the European Space Agency (ESA; contract nos. 4000112019/14/NL/CT (CLARA), 4000134661/21/NL/AD (CARDINAL), and 4000133155/20/NL/FF/tfd (ICERAD)).

References

Barker, H. W., Wiellicki, B. A., and Parker, L.: A Parameterization for Computing Grid-Averaged Solar Fluxes for Inhomogeneous Marine Boundary Layer Clouds. Part II: Validation Using Satellite Data, Journal of the Atmospheric Sciences, 53, 2304–2316, https://doi.org/10.1175/1520-0469(1996)053<2304:APFCGA>2.0.CO;2, publisher: American Meteorological Society Section: Journal of the Atmospheric Sciences, 1996.

Barker, H. W., Goldstein, R. K., and Stevens, D. E.: Monte Carlo Simulation of Solar Reflectances for Cloudy Atmospheres, Journal of the Atmospheric Sciences, 60, 1881–1894, https://doi.org/10.1175/1520-0469(2003)060<1881:MCSOSR>2.0.CO;2, publisher: American Meteorological Society Section: Journal of the Atmospheric Sciences, 2003.

Brenguier, J.-L., Pawlowska, H., Schüller, L., Preusker, R., Fischer, J., and Fouquart, Y.: Radiative Properties of Boundary Layer Clouds: Droplet Effective Radius versus Number Concentration, Journal of the Atmospheric Sciences, 57, 803–821, https://doi.org/10.1175/1520-0469(2000)057<0803:RPOBLC>2.0.CO;2, 2000.

Coakley, J. A. and Chylek, P.: The Two-Stream Approximation in Radiative Transfer: Including the Angle of the Incident Radiation, Journal of the Atmospheric Sciences, 32, 409–418, https://doi.org/10.1175/1520-0469(1975)032<0409:ttsair>2.0.co;2, 1975.

Cole, J. N. S., Barker, H. W., Qu, Z., Villefranque, N., and Shephard, M. W.: Broadband radiative quantities for the EarthCARE mission: the ACM-COM and ACM-RT products, Atmospheric Measurement Techniques, 16, 4271–4288, https://doi.org/10.5194/amt-16-4271-2023, 2023.

Dewitte, S., Gonzalez, L., Clerbaux, N., Ipe, A., Bertrand, C., and De Paepe, B.: The Geostationary Earth Radiation Budget Edition 1 data processing algorithms, Advances in Space Research, 41, 1906–1913, https://doi.org/10.1016/j.asr.2007.07.042, 2008.

Domenech, C. and Wehr, T.: Use of Artificial Neural Networks to Retrieve TOA SW Radiative Fluxes for the EarthCARE Mission, IEEE Transactions on Geoscience and Remote Sensing, 49, 1839–1849, https://doi.org/10.1109/tgrs.2010.2102768, 2011.

Forster, P., Storelvmo, T., Armour, K., Collins, W., Dufresne, J.-L., Frame, D., Lunt, D. J., Mauritsen, T., Palmer, M. D., Watanabe, M., Wild, M., and Zhang, H.: The Earth's Energy Budget, Climate Feedbacks, and Climate Sensitivity, in: Climate Change 2021: The Physical Science Basis. Contribution of Working Group I to the Sixth Assessment Report of the Intergovernmental Panel on Climate Change, edited by Masson-Delmotte, V., Zhai, P., Pirani, A., Connors, S. L., Péan, C., Berger, S., Caud, N., Chen, Y., Goldfarb, L., Gomis, M. I., Huang, M., Leitzell, K., Lonnoy, E., Matthews, J. B. R., Maycock, T. K., Waterfield, T., Yelekçi, O., Yu, R., and Zhou, B., pp. 923–1054, Cambridge University Press, Cambridge, United Kingdom and New York, NY, USA, https://doi.org/10.1017/9781009157896.009, 2021.

Gristey, J. J., Su, W., Loeb, N. G., Vonder Haar, T. H., Tornow, F., Schmidt, S. K., Hakuba, M. Z., Pilewskie, P., and Russell, J. E.: Shortwave radiance to irradiance conversion for Earth radiation budget satellite observations: A review, MDPI Remote Sensing, 13, 2640, https://doi.org/10.3390/rs13132640, 2021.

Loeb, N. G. and Manalo-Smith, N.: Top-of-Atmosphere Direct Radiative Effect of Aerosols over Global Oceans from Merged CERES and MODIS Observations, Journal of Climate, 18, 3506–3526, https://doi.org/10.1175/jcli3504.1, 2005.

Loeb, N. G., Manalo-Smith, N., Kato, S., Miller, W. F., Gupta, S. K., Minnis, P., and Wielicki, B. A.: Angular Distribution Models for Top-of-Atmosphere Radiative Flux Estimation from the Clouds and the Earth's Radiant Energy System Instrument on the Tropical Rainfall Measuring Mission Satellite. Part I: Methodology, Journal of Applied Meteorology, 42, 240–265, https://doi.org/10.1175/1520-0450(2003)042<0240:admfto>2.0.co;2, 2003.

Loeb, N. G., Kato, S., Loukachine, K., and Manalo-Smith, N.: Angular Distribution Models for Top-of-Atmosphere Radiative Flux Estimation from the Clouds and the Earth's Radiant Energy System Instrument on the Terra Satellite. Part I: Methodology, Journal of Atmospheric and Oceanic Technology, 22, 338–351, https://doi.org/10.1175/jtech1712.1, 2005a.

Loeb, N. G., Kato, S., Loukachine, K., and Manalo-Smith, N.: Angular Distribution Models for Top-of-Atmosphere Radiative Flux Estimation from the Clouds and the Earth's Radiant Energy System Instrument on the *Terra* Satellite. Part I: Methodology, Journal of Atmospheric and Oceanic Technology, 22, 338–351, https://doi.org/10.1175/JTECH1712.1, 2005b.

Marchuk, G. I., Mikhailov, G. A., Nazaraliev, M. A., Darbinjan, R. A., Kargin, B. A., and Elepov, B. S.: Monte Carlo Methods in Atmospheric Optics, in: Optical Science Series, Springer Verlag, 12, 208 pp, https://doi.org/https://doi.org/10.1007/978-3-540-35237-2, 1980.

Mayer, B., Schröder, M., Preusker, R., and Schüller, L.: Remote sensing of water cloud droplet size distributions using the backscatter glory: a case study, Atmospheric Chemistry and Physics, 4, 1255–1263, https://doi.org/10.5194/acp-4-1255-2004, 2004.

Smith, G. L., Green, R. N., Raschke, E., Avis, L. M., Suttles, J. T., Wielicki, B. A., and Davies, R.: Inversion methods for satellite studies of the Earth's Radiation Budget: Development of algorithms for the ERBE Mission, Reviews of Geophysics, 24, 407–421, https://doi.org/10.1029/rg024i002p00407, 1986.

Su, W., Corbett, J., Eitzen, Z., and Liang, L.: Next-generation angular distribution models for top-of-atmosphere radiative flux calculation from CERES instruments: methodology, Atmospheric Measurement Techniques, 8, 611–632, https://doi.org/10.5194/amt-8-611-2015, 2015.

Tornow, F., Preusker, R., Domenech, C., Henken, C., and Testorp, S.: Top-of-Atmosphere Shortwave Anisotropy over Liquid Clouds: Sensitivity to Clouds' Microphysical Structure and Cloud-Topped Moisture, Atmosphere, 9, https://doi.org/10.3390/atmos9070256, 2018.

Tornow, F., Domenech, C., and Fischer, J.: On the Use of Geophysical Parameters for the Top-of-Atmosphere Shortwave Clear-Sky Radiance-to-Flux Conversion in EarthCARE, Journal of Atmospheric and Oceanic Technology, 36, 717–732, https://doi.org/10.1175/jtech-d-18-0087.1, 2019.

Tornow, F., Domenech, C., Barker, H. W., Preusker, R., and Fischer, J.: Using two-stream theory to capture fluctuations of satellite-perceived TOA SW radiances reflected from clouds over ocean, Atmospheric Measurement Techniques, 13, 3909–3922, https://doi.org/10.5194/amt-13-3909-2020, 2020.

Tornow, F., Domenech, C., Cole, J. N. S., Madenach, N., and Fischer, J.: Changes in TOA SW Fluxes over Marine Clouds When Estimated via Semi-Physical Angular Distribution Models, Journal of Atmospheric and Oceanic Technology, https://doi.org/10.1175/JTECH-D-20-0107.1, 2021.

Velázquez Blázquez, A., Baudrez, E., Clerbaux, N., and Domenech, C.: Unfiltering of the EarthCARE Broadband Radiometer (BBR) observations: the BM-RAD product, Atmospheric Measurement Techniques, 17, 4245–4256, https://doi.org/10.5194/amt-17-4245-2024, 2024a.

Velázquez Blázquez, A., Domenech, C., Baudrez, E., Clerbaux, N., Salas Molar, C., and Madenach, N.: Retrieval of top-of-atmosphere fluxes from combined EarthCARE LiDAR, imager and broadband radiometer observations: the BMA-FLX product, Atmospheric Measurement Techniques, https://doi.org/10.5194/egusphere-2024-1539, 2024b.

Viollier, M., Standfuss, C., Chomette, O., and Quesney, A.: Top-of-Atmosphere Radiance-to-Flux Conversion in the SW Domain for the ScaRaB-3 Instrument on Megha-Tropiques, Journal of Atmospheric and Oceanic Technology, 26, 2161–2171, https://doi.org/10.1175/2009jtecha1264.1, 2009.

Wehr, T., Kubota, T., Tzeremes, G., Wallace, K., Nakatsuka, H., Ohno, Y., Koopman, R., Rusli, S., Kikuchi, M., Eisinger, M., Tanaka, T., Taga, M., Deghaye, P., Tomita, E., and Bernaerts, D.: The EarthCARE mission – science and system overview, Atmospheric Measurement Techniques, 16, 3581–3608, https://doi.org/10.5194/amt-16-3581-2023, 2023.

Wild, M., Folini, D., Hakuba, M. Z., Schär, C., Seneviratne, S. I., Kato, S., Rutan, D., Ammann, C., Wood, E. F., and König-Langlo, G.: The energy balance over land and oceans: an assessment based on direct observations and CMIP5 climate models, Climate Dynamics, 44, 3393–3429, https://doi.org/10.1007/s00382-014-2430-z, 2014.

Wild, M., Hakuba, M. Z., Folini, D., Dörig-Ott, P., Schär, C., Kato, S., and Long, C. N.: The cloud-free global energy balance and inferred cloud radiative effects: an assessment based on direct observations and climate models, Climate Dynamics, 52, 4787–4812, https://doi.org/10.1007/s00382-018-4413-y, 2018.

Wood, R.: Relationships between optical depth, liquid water path, droplet concentration and effective radius in an adiabatic layer cloud, Tech. rep., https://atmos.uw.edu/~robwood/papers/chilean_plume/optical_depth_relations.pdf, unpublished manuscript, 2006.

~~Flux deviations for scenarios with varying θ_s, θ_v, N_d and $\overline{\tau}$. The upper panel shows the results for the semi-physical approach and the lower panel the results for the sigmoidal approach.~~

Table A1. Table showing pre-selected $\overline{\tau}_{pre}$, ν_{pre} for the 25 scenes and the calculated $\overline{\tau}$, ν and $\overline{r}_{\mathrm{eff}}^{\mathrm{ctop}}$ after assigning the profiles to the boxes of MODIS observations with the most similar $\overline{\tau_{\mathrm{o}}}$, ν_{o} values. The calculated values are for the scenes with N_{d}=25.

Scene	$\overline{\tau}_{pre}$, ν_{pre}	$\overline{\tau_{\mathrm{o}}}$, ν_{o}	$\overline{\tau}$, ν	$\overline{r}_{\mathrm{eff}}^{\mathrm{ctop}}$
1	2.8, 1.1	4.2, 1.5	4.2, 1.7	15.9
2	2.8, 2.8	3.9, 2.7	3.8, 3.2	15.6
3	2.8, 4.6	3.6, 4.7	3.6, 5.3	15.4
4	2.8, 6.3	4.3, 7.8	4.3, 11.0	15.9
5	2.8, 8.0	4.4, 8.4	4.4, 8.7	16.0
6	4.5, 1.1	5.3, 1.1	5.2, 1.2	16.7
7	4.5, 4.6	4.4, 4.7	4.4, 4.9	16.0
8	4.5, 8.0	5.2, 7.8	5.2, 7.7	16.6
9	4.5, 11.5	4.4, 10.9	4.4, 10.5	16.0
10	4.5, 15.0	5.8, 15.5	5.8, 14.9	16.9
11	7.4, 1.1	7.8, 1.5	7.7, 1.5	18.0
12	7.4, 5.8	7.5, 5.8	7.5, 5.7	17.8
13	7.4, 10.5	7.4, 10.5	7.4, 10.5	17.8
14	7.4, 15.3	7.6, 15.1	7.6, 14.6	17.8
15	7.4, 20.0	6.6, 19.1	6.6, 19.0	17.4
16	12.2, 2.0	12.3, 2.3	12.3, 2.3	19.7
17	12.2, 7.8	12.0, 7.9	12.0, 7.8	19.6
18	12.2, 13.5	12.2, 13.6	12.2, 13.5	19.6
19	12.2, 19.2	11.9, 19.8	11.9, 19.3	19.5
20	12.2, 25.0	12.6, 24.1	12.6, 23.3	19.7
21	20.1, 5.0	18.8, 5.5	18.8, 5.5	21.4
22	20.1, 8.8	19.6, 9.1	19.6, 9.2	21.6
23	20.1, 12.5	21.5, 13.9	21.5, 14.0	22.0
24	20.1, 16.2	22.2, 14.6	22.2, 14.4	22.1
25	20.1, 20.0	20.3, 20.7	20.3, 20.3	21.7